

**ON MASS IN 4π SOLID ANGLE AROUND SONG CsI SCINTILLATOR ABOARD
CORONAS-I SATELLITE****R. Bučík^{1*,†}, K. Kudela^{2*}****Institute of Experimental Physics, SAS, Watsonova 47, 043 53 Košice, Slovak Republic**† Technical University in Zvolen, T.G. Masaryka 24, 960 53 Zvolen, Slovak Republic*

Received 10 January 2003 in final form 25 May 2003, accepted 30 May 2003

The complex geometric setup around the SONG CsI scintillator aboard the CORONAS-I satellite has been modelled, to evaluate the mass thickness passed through by the cosmic ray particle striking the detector. The analytic functional form giving the amount of matter traversed in absorbers for an arbitrary incident directions is present. The population mean and variance of the mass thickness are estimated by random sampling of the uniformly distributed particle trajectories in the several solid angles.

PACS: 95.55.-n, 02.70.-c

1 Introduction

SONG instrument aboard the CORONAS-I satellite has been primarily intended for detection of solar neutral radiation. To deal with the amount of matter in the region of the CsI scintillation crystal, which is the primary detecting element, we are motivated by knowledge of the local background conditions and of the detector field of view. For example, the measurement of the locally produced gamma rays is important at least for two reasons: (1) as a detector background in remotely monitoring of the electron precipitation events, and (2) for indirect investigation of the trapped electron population. Another important meaning of the knowledge of background situation is for the separation of the local contribution from the external gamma rays (e.g. those of solar origin). The determination of the field of view has a great importance, particularly for uncollimated detectors. In the following text we begin with a brief description of the experimental setup (Section 2). In Section 3, the model of the matter distribution on CORONAS-I satellite is described. Section 4 presents the method of the average mass thickness calculation by simple Monte Carlo integration. The last section (5) contains results (mean and variance) of the mass thickness simulations in the selected solid angles around the SONG CsI scintillator.

2 Experiment description

Low altitude satellite CORONAS-I has been devoted to the study of various aspects of solar activity. The SONG device is a part of the complex measuring high energy electromagnetic and corpuscular emissions from the Sun. The instrument consists of a phoswich type CsI(Tl) crystal

¹E-mail address: bucik@vsld.tuzvo.sk²E-mail address: kkudela@kosice.upjs.sk

scintillator (20 cm diameter \times 10 cm length) viewed by three photomultipliers. The whole scintillator counter is entirely surrounded by a 2 cm thick plastic scintillator anticoincidence shield for charged particles. The spectrometer has no collimator and the axis of the spectrometer is parallel to the longitudinal axis of the satellite. More details can be found in Baláž et al., 1994 [1].

The CORONAS-I satellite was launched on March 2, 1994 into a nearly circular orbit at an altitude of 500 km and an inclination of 83°. During its first working period (until July 5, 1994) CORONAS-I satellite was three-axis stabilized and was directed with its longitudinal axis towards the Sun. This was true for both day as well as night passes (SONG was oriented towards the Earth on night side of the orbit). The SONG device was mounted on the platform for the scientific instruments. The platform was placed at a distance of 1 m above the forward end of the satellite. The mass of the spacecraft was 2300 kg. It is cylindrical in shape, approximately 2.3 m in diameter and 5 m high. Extending from the satellite were long-wire antennas and solar panels with a total span of 12.8 m.

2.1 Scientific equipment on upper plate of CORONAS-I

A schematic configuration of the scientific equipment on the spacecraft instrument platform is shown in Fig. 1. Fig. 1a displays view from the front -parallel to the longitudinal satellite X -axis, and Fig. 1b view from the side -parallel to the satellite Y -axis. The forward end of the satellite body is indicated on the bottom of Fig. 1b. Due to the large linear size of some devices in the direction to the Sun, the instruments were situated in the holes on the plate to minimize their inertia moments relatively to the plate.

A list of all devices on the instrument platform and their corresponding masses are provided in Tab. 1. Notice that the masses of devices number 15 and 16 have been only estimated as a product of their approximate volume and mean device density. The last quantity is evaluated in the next section.

3 Model description

3.1 Model of the mass around the CsI crystal

3.1.1 Devices on the platform

The layout of all devices around the CsI on the upper platform was modelled by two homogeneous right circular cylinders: (1) cylinder located in the hemisphere above the center of the CsI and designated as C1 and (2) cylinder located in the opposite hemisphere and designated as C2. All we need now are the radii, heights and densities of the proposed cylinders.

To obtain the mean cylinder density we need to know the mass m_i and the volume V_i of the i th instrument or its part lying in the upper or lower hemispheres (uh or lh) according to equation

$$\varrho = \frac{\sum m_i}{\sum V_i} \quad (1)$$

Unfortunately, the devices dimensions are not readily available (except for the SONG instrument), so we take their from the sketch (Fig. 1). Moreover, only several instrument heights

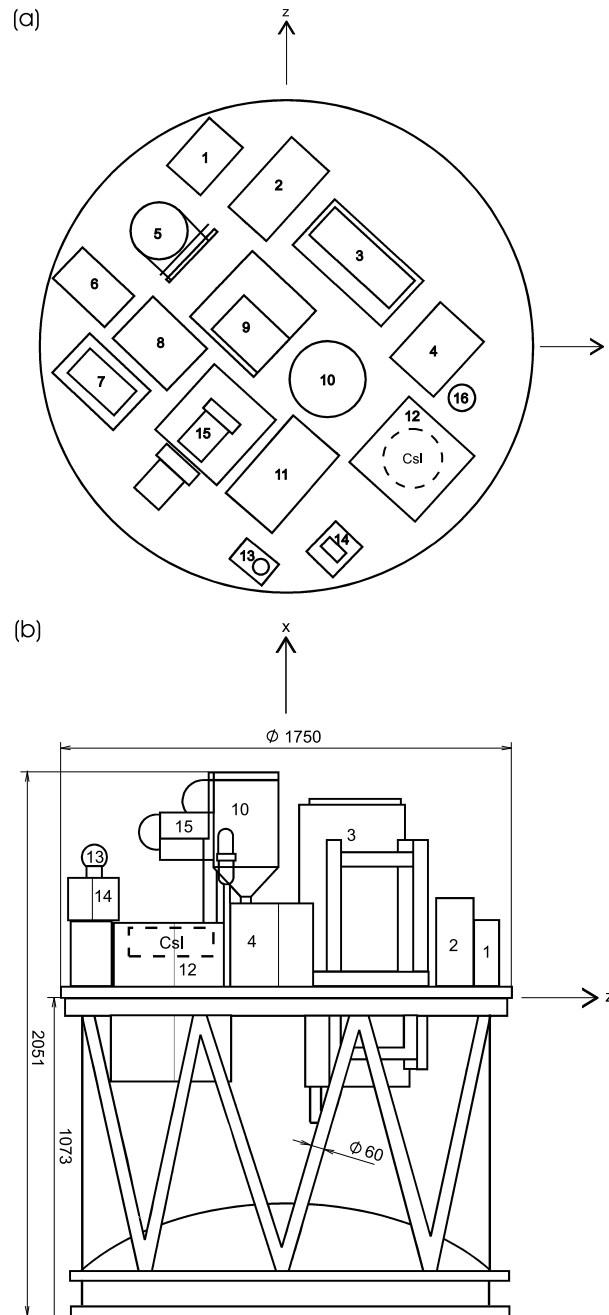


Fig. 1. Configuration of the scientific equipment on the instrument platform of the CORONAS-I satellite. (a) view from the front (normal view of y - z plane), (b) view from the side (normal view of x - z plane)

Label	Name	Mass (kg)
1	DIAGENNESS-BF	5.4
2	DIAGENNESS-BS	7.8
3	TEREK-BD	38.0
4	TEREK-BE2	7.5
5	VUSS	18.5
6	IRIS BV2	6.3
7	IRIS BV1	8.0
8	RES-K-BE2	7.5
9	RES-K-BD	37.2
10	GELIKON-D1	12.3
11	GELIKON-E	7.4
12	SONG-D	44.7
13	DIFOS-BF	4.1
14	SURF	3.6
15	The satellite service system	34.1
16	Thermodetector	1.8
Σ		244.2

Tab. 1. A list of all devices on the upper platform and their respective masses

(vertical dimensions) are visible in Fig. 1b. Therefore, the calculated cylinder density presents only crude approximation. The measurements obtained from Fig. 1 are summarized in Tab. 2. The labels of the visible instruments in Fig. 1b are shown in the column 2. The normally viewed surface area S_i (column 3) was taken from Fig. 1a and was considered the area of the base of the i th instrument on the platform. The fractional volume V_i has been computed as the product $S_i h_i$. The instrument heights were taken from Fig. 1b. Our simplifications suppose the homogeneity (i.e. constant density across the body) of all devices on the instrument platform. Under this assumption the fractional device mass m_i has been estimated to be proportional to the device height h_i in the particular hemisphere. By eq. (1), $\rho_1 = 0.28872 \text{ g cm}^{-3}$ and $\rho_2 = 0.34499 \text{ g cm}^{-3}$, the densities of the cylinders C1 and C2, respectively. Data given in Tab. 2 can also provide the overall mean device density on the instrument platform.

Since we have no informations about the heights of other devices than those given in Tab. 2 we only evaluate their possible maximal values. Taking into account the device arrangement on the upper platform (see Fig. 1) we get the following set of relations:

$$h_5 \leq h_1, h_6 \leq h_2, h_{7,8,9} \leq h_4, h_{15} \leq h_{10}, h_{11} \leq h_{12}, \quad (2)$$

where h_j indicates the height of the j th instrument and j refers to the instrument label on the platform.

Knowing the area of the cylinder base, we can determine the radius of the right circular cylinder. The areas of the bases of all devices on the instrument platform, which are listed in

i	Label	S_i (cm ²)	h_i (cm)		V_i (cm ³)		m_i (kg)	
			uh	lh	uh	lh	uh	lh
1	1	470.5	9.8	19.6	4602	9203	2.1	3.3
2	2	718.4	19.6	19.6	14051	14051	3.9	3.9
3	3	1181.3	60.8	63.0	71887	74453	18.7	19.3
4	4	661.7	17.4	19.6	11504	12942	3.6	3.9
5	12	1225.0	.0	54.3	0	66558	.0	30.7
6	13	163.8	41.3	19.6	6765	3204	2.8	1.3
7	14	231.1	28.3	19.6	6528	4519	2.2	1.4
Σ					115337	184930	33.3	63.8

Tab. 2. Summary of observations from Fig. 1.

Tab. 3 (the second column) have been evaluated from Fig. 1a. By summing up all these values, we find the area of the base of the cylinder C2. In case of the cylinder C1 we must exclude the areas of the bases of the devices labeled as 11 and 12, which entirely lie in the lower hemisphere. The calculated values of the radii are $r_1 = 53.19$ cm for C1 and $r_2 = 59.31$ cm for C2.

Tab. 3, column 3, gives the fractional instrument masses in the lower hemisphere, assuming again to be proportional to their respective heights. In case of the hidden devices in Fig. 1b, their heights have been taken according to the relations in (2). The last value in the rightmost column presents the mass m_2 of the cylinder C2. The mass m_1 of the cylinder C1 is found as follows.

$$m_1 = m_t - m_2 - m_{CsI}, \quad (3)$$

where m_t is the total mass of devices on the instrument platform (given in Tab. 1) and $m_{CsI} = 14$ kg is the mass of the CsI crystal.

The height of the right circular cylinder is given by

$$h = \frac{m}{S\rho} = \frac{m}{2\pi r\rho}, \quad (4)$$

where S , r , ρ and m have their common meaning. Eq. (4) yields the following cylinder heights: $h_1 = 40.99$ cm for C1 and $h_2 = 32.79$ cm for C2.

3.1.2 Instrument platform

The cylindrical aluminium platform (designated as C3) has 175 cm diameter and 1.2 cm height. Its calculated approximate mass m_3 has value of 78 kg.

3.1.3 Vehicle and rest mass

The cylindrical vehicle itself, the solar panels, antennas and instruments on the opposite end of the satellite were simulated by the right circular homogeneous cylinder (labeled as C4) with

Label	S_i (cm ²)	m_i (kg)
1	470.5	3.3
2	718.4	3.9
3	1181.3	19.3
4	661.7	3.9
5	427.6	11.4
6	433.5	3.2
7	672.2	4.2
8	548.2	3.9
9	1225.0	19.2
10	668.1	2.5
11	937.7	7.4
12	1225.0	30.7
13	163.8	1.3
14	231.1	1.4
15	1405.6	8.9
16	81.1	0.5
Σ	11050.8	125.0

Tab. 3. The summary of the areas S_i of device bases on the upper plate and the fractional instrument masses m_i in the lower hemisphere.

diameter of 2.3 m and height of 2.94 m . Knowing the values of its volume and mass (1978 kg), we have a mean density of $0.16193 \text{ g cm}^{-3}$. The mass of the proposed cylinder C4 was taken approximately to be

$$m_4 = M - m_t - m_3, \quad (5)$$

where M is the spacecraft mass (2300 kg), and m_t and m_3 have their previous meaning.

3.2 Model of geometry configuration

The proposed model of the geometrical setup of the matter distribution around the CsI crystal is shown in Fig. 2. The origin O of our reference system (a right-handed Cartesian coordinate system) is placed at the center of the CsI. Fig. 2a is the front view (parallel to the z -axis), and Fig. 2b is the cross sectional view (parallel to the x -axis). The center of the CsI crystal was located at a distance of 22.5 cm from the instrument platform and 129.8 cm from the vehicle, respectively. The offset of the CsI center from the vehicle and platform common axis was 56.5 cm.

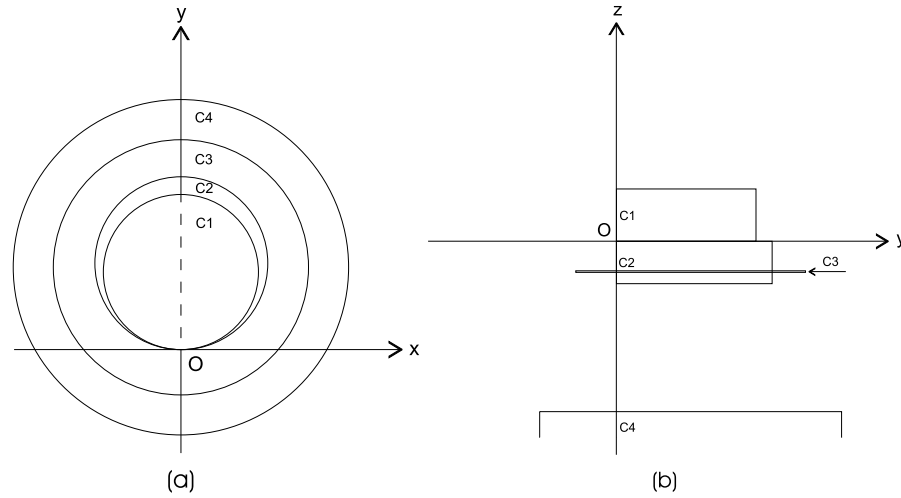


Fig. 2. Schematic of the model of the geometrical arrangement of the cylinders C1, C2, C3, and C4.

3.2.1 CsI solid angles

In configuration according to Fig. 2 we evaluate the solid angles subtended by the satellite body, instrument platform and both cylinders modeling the device arrangement on the platform. Consider first the vehicle and the instrument platform.

The solid angle Ω subtended by a surface A , in spherical coordinates, is given by

$$\Omega = \iint_A \sin \theta d\phi d\theta, \tag{6}$$

where θ is the polar angle and ϕ is the azimuth. Consider the base of the cylinder C3 or C4 with the center $S(0, y_S, z_S)$ and the radius r shown in Fig. 3 and assume that the origin O is located at the CsI center. Refer to Fig. 3, the surface A is bounded by a circle $x^2 + (y - y_S)^2 = r^2$. Written in spherical coordinates we have

$$\rho = \frac{y_S \sin \phi + \sqrt{r^2 - y_S^2 \cos^2 \phi}}{\sin \phi}. \tag{7}$$

The range of ϕ is from 0 to 2π . To find the range of θ we replace ρ with $z_S / \cos \theta$. Then

$$\tan \theta = \frac{y_S \sin \phi + \sqrt{r^2 - y_S^2 \cos^2 \phi}}{z_S}. \tag{8}$$

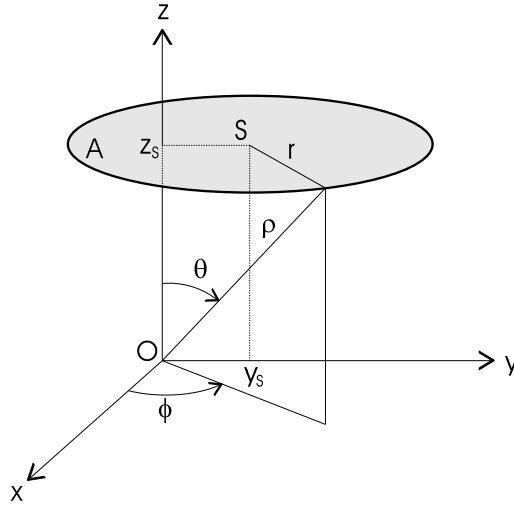


Fig. 3. The coordinate system in which the area A of the base of the right circular cylinder is defined.

Applying eq. (6) we obtain the following:

$$\begin{aligned} \Omega &= \int_0^{2\pi} d\phi \int_0^{\arctan((y_S \sin \phi + \sqrt{r^2 - y_S^2 \cos^2 \phi})/z_S)} \sin \theta d\theta \\ &= 2\pi - \int_0^{2\pi} \cos \left(\arctan \frac{y_S \sin \phi + \sqrt{r^2 - y_S^2 \cos^2 \phi}}{z_S} \right) d\phi. \end{aligned} \quad (9)$$

The last integral has been solved numerically by the Romberg's method (e.g. [2]) with a relative error less than 10^{-6} , using the IDL [3] routine NR_QROMB³. Thus, the solid angles subtended by the satellite body and the instrument platform are 0.45232π sr and 1.30588π sr, respectively. Note that the meaning of the constants y_S , z_S and r are the offset of the cylinder axis, distance between center of the CsI and the cylinder base, and the radius of the cylinder, respectively. All these quantities have been previously evaluated. Recall that the solid angle corresponding to the half hemisphere equals 1π steradians. Refer to Fig. 2, the cylinder C1 entirely lies in one half hemisphere and due to its special position, the solid angle being subtended is 1 sr. This is also case of the cylinder C2.

4 The average mass thickness in the modelled absorbers

In this section we evaluate the average mass thickness (in g cm^{-2}) in all suggested cylinders through which the cosmic ray particle must travel in order to reach the point detector (the center

³NR_QROMB is based on the routine `qr_omb` described in section 4.3 of Numerical Recipes in C: The Art of Scientific Computing [4].

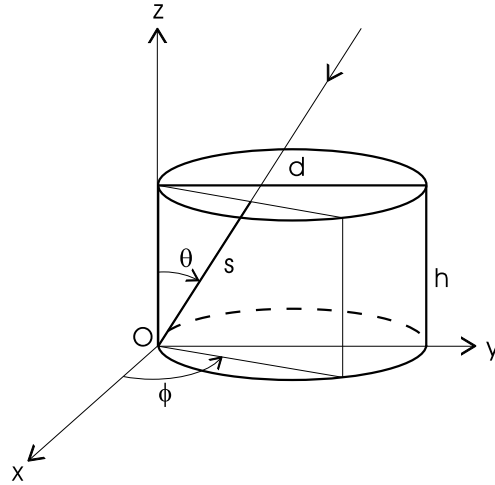


Fig. 4. The geometry used in deriving the pathlength $s(\theta, \phi)$ traversed in the cylinders C1 and C2.

of CsI). Due to proposed homogeneity of the simulated cylinders we deal with the pathlengths expressed in cm. Furthermore, the isotropy in propagating of the cosmic ray particles is supposed and for simplicity trajectories are assumed to be straight lines. The statement of the problem suggests using a Monte Carlo simulation.

4.1 Cylinders C1 and C2

Shown in Fig. 4, consider the right circular cylinder with the diameter d and the height h . Let the point detector be located at the origin O . The direction of incidence of the cosmic ray particle is defined by spherical coordinates (θ, ϕ) . The range of ϕ is $(0, \pi)$, and of θ $(0, \frac{\pi}{2})$. The pathlength of the trajectory that traverse the cylinder may be expressed as:

$$s(\theta, \phi) = \begin{cases} \frac{h}{\cos \theta} & \text{if } 0 < \theta \leq \arctan \frac{d \sin \phi}{h}, \\ \frac{d \sin \phi}{\sin \theta} & \text{otherwise.} \end{cases} \quad (10)$$

Assumed isotropy of the radiation implies the uniform frequency distribution of directions of incidence $D(\theta, \phi)$. The average pathlength \bar{s} is given by the first moment of the incident direction distribution.

$$\bar{s} = \iint s(\theta, \phi) D(\theta, \phi) d\theta d\phi \quad (11)$$

Above integral has been solved by the Monte Carlo technique (e.g. [5]). Its essential basis is the Strong Law of Large Numbers (SLLN) and the Central Limit Theorem (CLT).

The Khintchine SLLN assures that for n sufficiently large,

$$\bar{s} \approx \frac{1}{n} \sum_{i=1}^n s(\theta_i, \phi_i) \equiv \frac{1}{n} \sum_{i=1}^n s_i \equiv \bar{s}_n, \quad (12)$$

with probability close to one, when s_i are n independent, identically distributed (idd) random variables with finite mean \bar{s} . Here \bar{s}_n is the sample mean and

$$\sigma_n^2 = \frac{n}{n-1} \left(\frac{1}{n} \sum_{i=1}^n s_i^2 - \bar{s}_n^2 \right) \quad (13)$$

is the sample variance. Moreover, by the CLT, as n tends to infinity,

$$\frac{\bar{s}_n - \bar{s}}{\sigma} \sqrt{n} \quad (14)$$

approaches a standard Gaussian distribution, provided that σ (which is the standard deviation of a sequence idd random variables s_1, s_2, \dots, s_n), is finite and not zero. Finally, the maximum error ε of the estimate of the mean pathlength, under 95% chance of covering the value of \bar{s} , is given by

$$\varepsilon = 1.96 \frac{\sigma_n}{\sqrt{n}}, \quad (15)$$

where the population standard deviation σ is replaced by its consistent estimator σ_n .

The general procedure that we used may be outlined as follows:

- (i) Choose number of trials (or trajectories) n , e.g. 1000 and preliminary compute \bar{s}_n and σ_n by eq. (12) and (13) respectively.
- (ii) Choose relative accuracy, e.g. 10^{-2} and find the approximate sample size n by

$$n > \left[\frac{1.96\sigma_n}{10^{-2}\bar{s}_n} \right]^2. \quad (16)$$

- (iii) According to the step (ii) use n to compute \bar{s}_n (eq. (12)) as an unbiased estimate of true (population) mean pathlength \bar{s} with desired relative accuracy, and σ_n^2 (eq. (13)) as an unbiased estimator of variance σ^2 of the pathlengths about their population mean value.
- (iv) Calculate the average mass thickness (g cm^{-2}) as a product of the mean cylinder density ρ (g cm^{-3}) and mean pathlength \bar{s} (cm) traversed in the cylinder.

The heart of the problem is computing s_i . This is done as follows:

- (i) Choose a random trajectory striking the detector. Let ξ_1 and ξ_2 be two pseudorandom deviates drawn uniformly on $(0, 1)$, then

$$\phi = \xi_1\pi \quad \text{and} \quad \theta = \xi_2 \frac{\pi}{2}$$

define the direction of incidence.

- (ii) In this direction calculate pathlength s_i (eq. (10)).
- (iii) Repeat steps (i), (ii) n times.

Cylinder	$\bar{s}_n \varrho$	$\sigma_n \varrho$	$\varepsilon \varrho$
C1	15.60	7.04	0.16
C2	17.04	9.08	0.17

Tab. 4. The results of the simulation of mass thickness for the cylinders C1 and C2.

In this paper, all random deviates are generated using the IDL routine RANDOMU, which generates pseudorandom numbers uniformly distributed in the interval $(0, 1)$.

The results for both cylinders C1 and C2 are summarized in Tab. 4, and the mass thickness distributions are shown in Fig. 5. The table lists the average mass thickness $\bar{s}_n \varrho$, the (sample population) standard deviation $\sigma_n \varrho$, and the 1.96σ statistical uncertainty $\varepsilon \varrho$. All quantities are multiplied by ϱ to obtain results in g cm^{-2} . The apparent bimodal distribution structure is the property of the proposed cylindrical shape and depends upon the ratio of the diameter to the height.

The fundamental disadvantage of the simple Monte Carlo integration is that its accuracy increases only as the square root of n , the number of sampled points. To achieve higher accuracy the more advanced techniques of Monte Carlo integration (called *reduction of variance* in the literature) are available. Due to simplifications involved in the outlined problem we believe that our requirements on accuracy are quite sufficient.

Note, if the direction of cosmic ray particle is specified then the problem can be modified by modeling of the incident direction density $D(\theta, \phi)$ by the Gaussian distribution.

4.2 Cylinders C3 and C4

Shown in Fig. 6, consider the right circular cylinder with the radius r and height h . Let b denote the offset of the cylinder axis from the origin O , and let l be the distance between the cylinder lower base and the x - y plane.

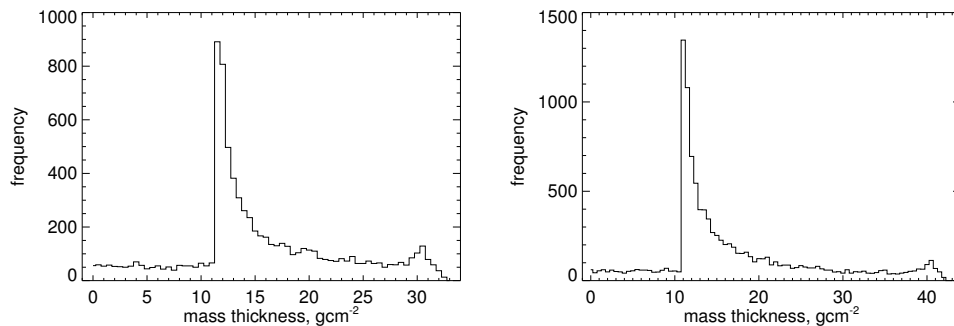


Fig. 5. Mass thickness distributions in the cylinders C1 (left) and C2 (right) for 7905 (C1), 10988 (C2) trajectories.

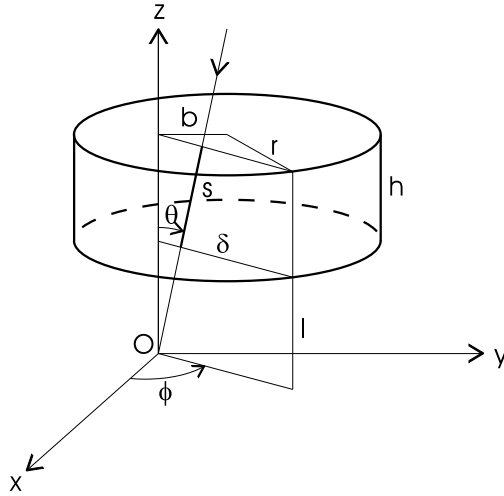


Fig. 6. The geometry used in deriving the pathlength $s(\theta, \phi)$ traversed in the cylinders C3 and C4.

The pathlength in the cylinder in Fig. 6 may be expressed as:

$$s(\theta, \phi) = \begin{cases} \frac{h}{\cos \theta} & \text{if } 0 < \theta \leq \arctan \frac{\delta}{h+l}, \\ \frac{\delta}{\sin \theta} - \frac{l}{\cos \theta} & \text{otherwise} \end{cases} \quad (17)$$

with

$$\delta = b \sin \phi + \sqrt{r^2 - b^2 \cos^2 \phi} \quad (18)$$

(cf. eq. (8)). The range of ϕ is $(0, 2\pi)$, and of θ $(0, \arctan \frac{\delta}{l})$.

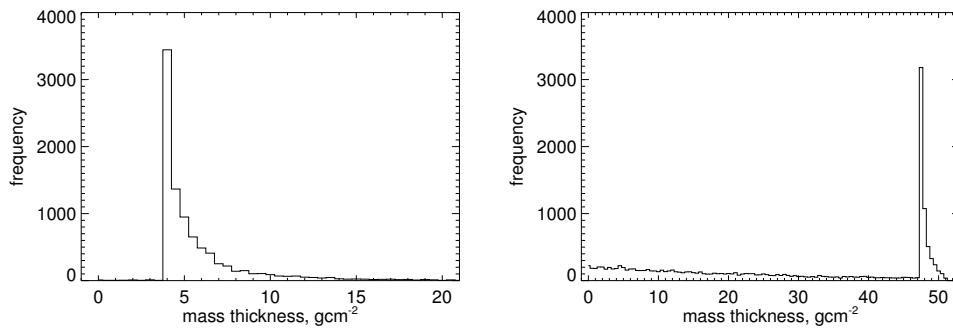


Fig. 7. Mass thickness distributions in the cylinders C3 (left) and C4 (right) for 9079 (C3), 15214 (C4) trajectories.

Cylinder	$\bar{s}_n \varrho$	$\sigma_n \varrho$	$\varepsilon \varrho$
C3	4.75	2.29	0.05
C4	29.00	18.08	0.29

Tab. 5. The results of the simulation of mass thickness for the cylinders C3 and C4.

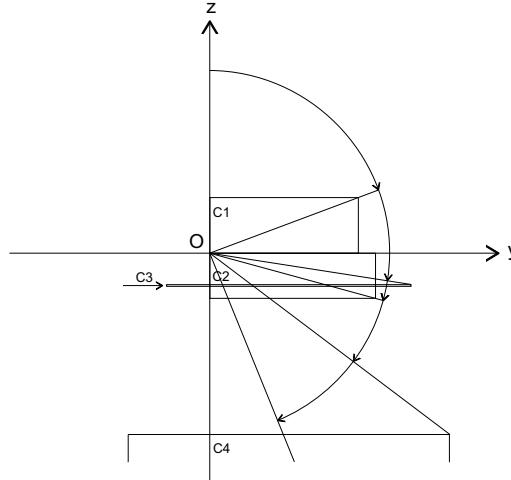


Fig. 8. A model of geometry in the region of the CsI scintillator (introduced in Section 3.2). The polar angles subtended by the bases of the modelled cylinders are denoted as θ_1 (upper base of C1), θ_2 (upper base of C3), θ_3 (lower base of C3), θ_4 (upper base of C4), θ_5 (lower base of C2), and θ_6 (lower base of C4).

The random direction of incidence is defined by

$$\phi = \xi_1 2\pi \quad \text{and} \quad \theta = \xi_2 \arctan \frac{\delta}{l}.$$

The results of the simulation are summarized in Tab. 5, and mass thickness distributions are shown in Fig. 7.

5 Mass thickness in space around detector

In this section we find the functional form describing the mass thickness over the whole space around the point detector. We consider this as a rough approximation of true mass thickness near the SONG CsI scintillator on CORONAS-I. For practical application we also evaluate the mean amount of matter in the selected solid angles by the method developed in the preceding section.

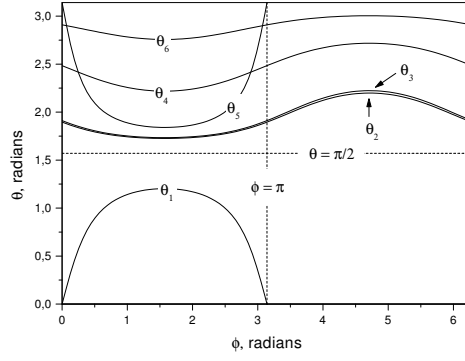


Fig. 9. A schematic diagram showing how polar angles subtended by cylinder bases depend on azimuth ϕ .

5.1 The mass thickness definition

Shown in Fig. 8, consider the model of geometry in the region of the point detector introduced in Section 3.2. To be more illustrative we diagrammatically give (Fig. 9) an azimuth dependence of the polar angles subtended by the modelled cylinders. In configuration depicted in Fig. 8, the amount of matter (in g cm^{-2}) traversed by the cosmic ray particle striking the detector, located at the origin O of our reference system, may be expressed as:

$$s(\theta, \phi) = \begin{cases} \eta_1 & 0 < \theta \leq \theta_1 & 0 < \phi \leq \pi \\ \nu_1 & \theta_1 < \theta \leq \frac{\pi}{2} & 0 < \phi \leq \pi \\ 0 & 0 < \theta \leq \frac{\pi}{2} & \pi < \phi < 2\pi \\ \nu_2 & \frac{\pi}{2} < \theta \leq \theta_2 & 0 < \phi \leq \pi \\ 0 & \frac{\pi}{2} < \theta \leq \theta_2 & \pi < \phi < 2\pi \\ \nu_2 + \tau_3 & \theta_2 < \theta \leq \theta_3 & 0 < \phi \leq \pi \\ \tau_3 & \theta_2 < \theta \leq \theta_3 & \pi < \phi < 2\pi \\ \nu_2 - \eta_3 & \theta_3 < \theta \leq \theta_4 & 0 < \phi \leq \phi_1 \vee \phi_2 < \phi \leq \pi \\ -\eta_3 & \theta_3 < \theta \leq \theta_4 & \pi < \phi < 2\pi \\ \nu_2 - \eta_3 & \theta_3 < \theta \leq \theta_5 & \phi_1 < \phi \leq \phi_2 \\ \nu_2 - \eta_3 + \tau_4 & \theta_4 < \theta \leq \theta_6 & 0 < \phi \leq \phi_3 \vee \phi_4 < \phi \leq \pi \\ \nu_2 - \eta_3 + \tau_4 & \theta_4 < \theta \leq \theta_5 & \phi_3 < \phi \leq \phi_1 \vee \phi_2 < \phi \leq \phi_4 \\ -\eta_2 - \eta_3 + \tau_4 & \theta_5 < \theta \leq \theta_6 & \phi_3 < \phi \leq \phi_1 \\ -\eta_2 - \eta_3 + \tau_4 & \theta_4 < \theta \leq \theta_6 & \phi_1 < \phi \leq \phi_2 \\ -\eta_3 + \tau_4 & \theta_4 < \theta \leq \theta_6 & \pi < \phi < 2\pi \\ \nu_2 - \eta_3 - \eta_4 & \theta_6 < \theta \leq \theta_5 & 0 < \phi \leq \phi_3 \vee \phi_4 < \phi \leq \pi \\ -\eta_2 - \eta_3 - \eta_4 & \theta_6 < \theta < \pi & \phi_3 < \phi \leq \phi_4 \\ -\eta_3 - \eta_4 & \theta_6 < \theta < \pi & \pi < \phi < 2\pi \end{cases} \quad (19)$$

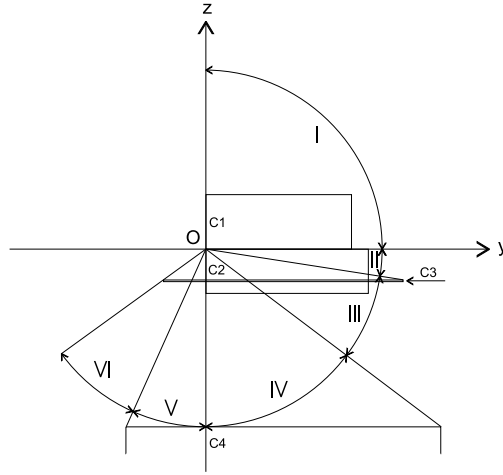


Fig. 10. Illustrating the solid angles selection.

with

$$\eta = \rho \frac{h}{\cos \theta}, \nu = \rho \frac{d \sin \phi}{\sin \theta}, \text{ and } \tau = \rho \left(\frac{\delta}{\sin \theta} - \frac{l}{\cos \theta} \right),$$

and

$$\theta_1 = \arctan \nu_1, \theta_2 = \pi - \arctan \frac{\delta_3}{l_3}, \theta_3 = \pi - \arctan \frac{\delta_3}{l_3 + h_3},$$

$$\theta_4 = \pi - \arctan \frac{\delta_4}{l_4}, \theta_5 = \pi - \arctan \nu_2, \theta_6 = \pi - \arctan \frac{\delta_4}{l_4 + h_4},$$

$$\phi_{1,2} = \arccos \left(\pm \sqrt{\frac{(r_4 h_2)^2 - (l_4 d_2 - b h_2)^2}{(b h_2)^2 - (l_4 d_2 - b h_2)^2}} \right),$$

$$\phi_{3,4} = \arccos \left(\pm \sqrt{\frac{(r_4 h_2)^2 - (l_4 d_2 + h_4 d_2 - b h_2)^2}{(b h_2)^2 - (l_4 d_2 + h_4 d_2 - b h_2)^2}} \right),$$

where $\phi_{1,2}$ and $\phi_{3,4}$ are ϕ -coordinates of θ_4 and θ_5 , and θ_5 and θ_6 intersections, respectively. The subscripts 1, 2, 3 and 4 refer to the cylinders C1, C2, C3, and C4 respectively. All other symbols have been previously defined.

5.2 The average mass thickness in the selected solid angles

As an example, the selection of the solid angles may be done according to the number of different absorbers lying in the individual quadrants, what is demonstrated in Fig. 10. The results of the Monte Carlo simulations in selected solid angles are summarized in Tab. 6. The solid angles Ω , given in the column 4 have been found by solving eq. (9). Tab. 7 lists results for another choice of the solid angles.

Design.	θ	ϕ	Ω	\bar{s}_n	σ_n	ε	n
I	$(0, \frac{\pi}{2})$	$(0, \pi)$	1.00π	15.60	7.04	0.16	7905
II	$(\frac{\pi}{2}, \theta_2)$	$(0, \pi)$	0.20π	26.09	12.73	0.26	9273
III	(θ_2, θ_4)	$(0, \pi)$	0.47π	30.34	12.44	0.30	6480
IV	(θ_4, π)	$(0, \pi)$	0.33π	45.87	17.87	0.46	5879
V	(θ_4, π)	$(\pi, 2\pi)$	0.13π	30.39	18.06	0.30	13573
VI	(θ_2, θ_4)	$(\pi, 2\pi)$	0.38π	4.66	1.07	0.05	2065

Tab. 6. The results of the simulation of mass thickness in selected solid angles. Listed are: θ, ϕ range, the solid angle Ω (sr), the average mass thickness \bar{s}_n (g cm^{-2}), the standard deviation σ_n (g cm^{-2}), 1.96σ statistical error ε (g cm^{-2}), and the number of trajectories n .

	θ	ϕ	\bar{s}_n	σ_n	ε	n
Lower right quadrant	$(\frac{\pi}{2}, \pi)$	$(0, \pi)$	37.66	18.01	0.38	8831
Lower left quadrant	$(\frac{\pi}{2}, \pi)$	$(\pi, 2\pi)$	11.25	16.54	0.11	83675
Upper hemisphere	$(0, \frac{\pi}{2})$	$(0, 2\pi)$	7.79	9.26	0.08	54590
Lower hemisphere	$(\frac{\pi}{2}, \pi)$	$(0, 2\pi)$	24.44	21.74	0.24	30468
4π solid angle	$(0, \pi)$	$(0, 2\pi)$	16.24	18.75	0.16	51314

Tab. 7. The results of the simulation of mass thickness in selected solid angles. Listed are: θ, ϕ range, the average mass thickness \bar{s}_n (g cm^{-2}), the standard deviation σ_n (g cm^{-2}), 1.96σ statistical error ε (g cm^{-2}), and the number of trajectories n .

6 Conclusion

The proposed model of the experimental setup around the CsI scintillation crystal on the CORONAS-I satellite can provide the basis for more sophisticated approach. Whatever next improvements should take into account the real variation of the density of matter near the CsI. The simulated results will also be checked after completing the information on the instruments dimensions and their masses.

Through all this paper we deal with the term *the mass thickness traversed in the absorber*, with the restriction that the particles of radiation travel in the straight lines. Since the incident trajectories are proposed to be uniformly distributed, this term has an another important interpretation, namely *the mass thickness viewed by the detector*. Thus, an amount of matter passed through by the particle can be solved by a more advanced method, called the particle transport technique.

The approach developed in this paper can be directly applicable to determine the passive shielding for the continuing CORONAS experiment, launching of the CORONAS-F satellite on July 31, 2001, with the improved version of the SONG instrument.

Acknowledgement: We wish to acknowledge to A. Luchaniniov and V. Butsik, Yuzhnoe Design Bureau, Dnepropetrovsk, for providing the scheme of the scientific equipment platform of the CORONAS-I satellite. We would like to thank S. P. Ryumin, Institute of Nuclear Physics, Moscow State University, for his many helpful comments.

This work was supported within the Institute of Experimental Physics, SAS, by VEGA grant 2/1147/21.

References

- [1] J. Baláž, A. V. Dmitriev, M. A. Kovalevskaya, K. Kudela, S. N. Kuznetsov, I. N. Myagkova, Yu. I. Nagornikh, J. Rojko, S. P. Ryumin: in *IAU Colloq. 144 "Solar Coronal Structures"*, ed. V. Rušin, P. Heinzel, J. C. Vial, VEDA, Bratislava 1994, p. 635
- [2] A. Ralston, P. Rabinowitz: *A First Course in Numerical Analysis*, MacGraw-Hill, New York 1978
- [3] *IDL*, Research Systems, Inc., Boulder 1992
- [4] W. H. Press, S. A. Teukolsky, W. T. Vetterling, B. P. Flannery: *Numerical Recipes in C: The Art of Scientific Computing*, Cambridge University Press, Cambridge 1992
- [5] N. P. Buslenko, Yu. A. Schreyder: *Monte Carlo Methods*, Fizmatgiz, Moscow 1961 (in Russian)